Crustal intrinsic and scattering attenuation of high-frequency shear waves in the contiguous United States

Tom Eulenfeld[1,2] **and Ulrich Wegler**[2]

[1]Federal Institute for Geosciences and Natural Resources, Hannover, Germany.
[2]Institute for Geosciences, Friedrich Schiller University of Jena, Jena, Germany.

Key Points:

- First maps of separated intrinsic and scattering attenuation as well as site amplification of high frequency S-waves (1–20 Hz)
- Contrast of intrinsic attenuation, scattering attenuation and site amplification for frequencies higher than 2 Hz between west and east
- Estimation of seismic moments and moment magnitudes for small earthquakes (M 1.5 – M 3.5)

Corresponding author: Tom Eulenfeld, `tom.eulenfeld@uni-jena.de`

Abstract

We use 10 years of data of the USArray project to estimate the areal distribution of crustal intrinsic and scattering attenuation of shear waves for frequencies between 1 Hz and 20 Hz in the contiguous United States. Additionally, we report energy site amplification factors and estimate moment magnitudes for small earthquakes (M 1.5 – M 3.5). The *Qopen* method is used to invert for intrinsic and scattering attenuation for each event and nearby stations. Observations are collected for around 25 000 events, averaged at each station and interpolated between station locations. In a second inversion, energy site amplifications and moment magnitudes are corrected by assuming, that site amplifications for one station and frequency are the same for different earthquakes. We observe a west-east decline of intrinsic attenuation for high frequencies which reflects the west-east transition from young, hot to old and cold crust. Scattering attenuation for high frequencies is stronger in the east with an extraordinary high attenuation around the southern part of the Appalachian Highlands and the Interior Low Plateaus. Results at low frequencies do not show clear trends. A large site amplification is observed at high frequencies in parts of the eastern United States. Estimated moment magnitudes show a good agreement to moment magnitudes independently derived from moment tensor inversion. Moment magnitudes in the west are higher than in the east for the same Richter magnitudes.

1 Introduction

The Transportable Array (TA) is one of the main components of the USArray project. It consists of around 400 installations which migrated eastwards over the continental United States between 2005 and 2015. The spacing between the TA stations is around 70 km. The Reference Network (RN) ties together the stations of the TA which partially do not have overlapping operation periods. It consists of more than 100 fixed stations at a spacing of around 300 km.

The dense seismic networks of the USArray project allow amongst others for large-scale, high resolution maps of seismic velocity distributions [e.g. *Burdick et al.*, 2008; *Yang and Ritzwoller*, 2008; *Lin et al.*, 2012]. For a precise description of wave propagation not only wave speed but attenuation of seismic waves is important. Two different mechanisms, besides geometrical spreading, have to be distinguished. Intrinsic attenuation which accounts for the conversion of seismic energy into different types of energy (e.g. heat) and scattering attenuation which describes the redistribution of seismic energy into different directions. Scattering and intrinsic attenuation are quantified by the transport scattering coefficient g^* and absorption coefficient b. The relation between those coefficients and the respective Q values Q_{sc} and Q_i is given by

$$Q_{sc}^{-1} = \frac{g^* v_0}{2\pi f} \qquad\qquad Q_i^{-1} = \frac{b}{2\pi f} \qquad (1)$$

with mean velocity v_0 and frequency f. We always refer to inverse Q values as these are proportional to attenuation strength. The total attenuation Q_{tot}^{-1} can be calculated by summing up individual contributions of scattering and intrinsic attenuation: $Q_{tot}^{-1} = Q_{sc}^{-1} + Q_i^{-1}$. The seismic albedo $B = Q_{sc}^{-1}/Q_{tot}^{-1}$ refers to the share of scattering attenuation in total attenuation.

Scattering properties of the medium for shear waves can be determined by analyzing the direct S-wave and its coda. The influence of compressional waves may be neglected in the S coda because of the high P-to-S conversion ratio. Intrinsic and scattering attenuation of shear waves are distinguished by their different impact on the energy envelope. While scattering influences the shape of the envelope in space and time – most notably the energy level between direct S-wave and scattered coda wave – intrinsic attenuation can be accounted for by an exponential decrease of the envelope with time. Basically two methods evolved for the separation of intrinsic and scattering attenuation of shear waves using homogeneous random media: *MLTWA* (Multiple lapse time window analysis) developed by *Hoshiba et al.* [1991] and *Fehler et al.* [1992], and *Qopen* (Separation of intrinsic and scattering Q by envelope

inversion) presented by *Eulenfeld and Wegler* [2016] and based upon *Sens-Schönfelder and Wegler* [2006]. Both methods invert for attenuation properties by comparing observed and modeled energy envelopes. The major difference is the selection and specific handling of envelope segments. MLTWA uses averaged data inside three or more time windows to calculate energy ratios for the inversion. Qopen uses adjustable windows for direct wave and coda, but data is not averaged inside the coda window. Another difference is that coda normalization is usually employed before MLTWA, while site amplifications and spectral source energies are a by-product of the inversion with the Qopen method. This allows for the computation of moment magnitudes for small earthquakes. It should be emphasized, that the assumption of an homogeneous scattering model neglects any depth dependence of Q values and seismic velocity [*Lacombe et al.*, 2003].

Carcolé and Sato [2010] used Hi-net data of more than 135 000 events to compile maps of intrinsic and scattering attenuation of shear waves for Japan for different frequency bands. MLTWA was used to separate attenuation for individual events at nearby stations. After that, averaging and interpolation was performed. In this study, we compile similar maps for the contiguous United States using the Qopen method and USArray data. Additionally, maps of energy site amplification are presented. Estimated moment magnitudes M_w are compared with results of independent moment tensor inversions and with Richter magnitudes M_R.

2 Data and method

### 2.1 Obtaining the target observables for a single earthquake

Data processing starts by inverting data from each considered frequency band and from each considered earthquake for the inverse of the quality factor for intrinsic attenuation Q_i^{-1}, the inverse of the quality factor for scattering attenuation Q_{sc}^{-1}, the energy site amplification factor R and the spectral source energy W. The observables Q_i^{-1}, Q_{sc}^{-1} and R are then assigned to the stations used in the particular inversion. After processing all events, energy site amplification measurements R are corrected by the procedure described in section 2.2. Finally, values of Q_i^{-1}, Q_{sc}^{-1} and R collected at each station are averaged and interpolated. Number of observations (n_{obs}) at each station is reported, too.

The inversion compares observed total energy envelopes E_{obs} of an individual event to modeled energy envelopes. The modeled energy envelopes at station i are calculated by [compare *Eulenfeld and Wegler*, 2016, eq. 1]

$$E_{mod}(t, \boldsymbol{r}_i) = W R_i G(t, \boldsymbol{r}_i, g^*) \, e^{-bt} \,. \tag{2}$$

t is the lapse time, $\boldsymbol{r}_i$ the vector pointing from the hypocenter to the station location, and W is the spectral source energy of the event. e^{-bt} describes the exponential intrinsic damping with time. The energy Green's function $G(t, \boldsymbol{r}_i, g^*)$ accounts for the direct wave and the scattered wave field. The most simple approach, which is also pursued in this paper, employs the analytic approximation of the solution for 3-dimensional isotropic radiative transfer to calculate the Green's function [*Paasschens*, 1997; *Eulenfeld and Wegler*, 2016, eq. 2]. The usage of an isotropic description of scattering can be justified also for anisotropic scattering as *Gaebler et al.* [2015] discussed exemplary that a scattering coefficient g_0 determined under the assumption of isotropic scattering can be directly translated to the transport scattering coefficient g^* in an anisotropic scattering medium ($g^*=g_0$). Observed energy densities corrected due to the free surface [*Eulenfeld and Wegler*, 2016, eq. 4] are inverted for g^*, b, W, and R_i with the Qopen method. g^* and b can be converted to Q values with equation 1.

We use data from 1844 stations of the transportable array and the reference network of the USArray program (virtual network codes _US–TA and _US–REF). Earthquake localizations and picks are taken from the catalog of the Array Network Facility (ANF) [*Astiz et al.*, 2014]. We analyze around 45 000 events of the time period between 04/01/2005 and
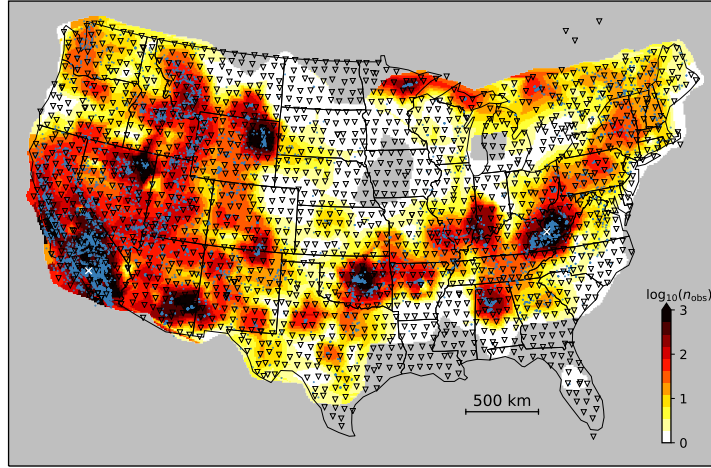
Figure 1. Map of used USArray stations (triangles) and earthquakes (blue dots). Color refers to the interpolated number of observations at 6 Hz on a logarithmic scale. White crosses mark the two earthquakes for which envelope fits are shown in figure 2.

08/31/2015 (more than 10 years) with magnitudes between 1.5 and 3.5 and a depth smaller than 40 km. Magnitude and depth constraints are the same as in *Carcolé and Sato* [2010]. Magnitudes are sufficient small to justify the assumption that earthquake source time functions can be approximated by a delta peak in space and time. The depth constraint guarantees events to be located inside or immediately under the crust. A plot of used stations and events is displayed in Figure 1.

For each event, stations with a distance smaller than 110 km are selected. Data for these stations is requested from IRIS with 40 Hz sampling rate and processed with the Qopen script hosted at `https://github.com/trichter/qopen`. The processing is detailed in *Eulenfeld and Wegler* [2016] and shortly recapitulated with adaptations for our use case: S-onset and P-onset at each station are obtained from the ANF picks. The mean S-wave velocity, which is important for calculation of theoretical Green's functions, is calculated from the S picks at the used stations. Data is filtered with a Butterworth bandpass filter in octave frequency bands (i.e. the higher corner frequency is twice the value of the lower corner frequency) with central frequencies at 1.5 Hz, 2.1 Hz, 3.0 Hz, 4.2 Hz, 6.0 Hz, 8.5 Hz, 12.0 Hz, and 17.0 Hz. For the highest central frequency, data is filtered with a Butterworth highpass filter with a corner frequency at 11.3 Hz. The filters are of order 2 and are applied once forward and once backward to guarantee zero phase shift. The further processing is applied separately for each frequency band. Energy envelopes are calculated with the help of the Hilbert transform. At each station, the average of the envelope is calculated in each of the time windows (−50 s; −40 s), (−40 s; −30 s), (−30 s; −20 s), and (−20 s; −10 s) relative to P-onset and the minimum of those averages is used as the envelope noise level which is subtracted from the envelope data. The direct S-wave window starts 0.2 s before the S-onset and has a length of 10 s. The coda window starts at the end of the corresponding direct wave window and ends 100 s after the S-onset or until the envelope falls under a level of 4 times the signal-to-noise ratio. Additionally, the coda is cut at the smallest possible local minimum if envelope data at a subsequent local maximum is larger by a factor of 4. This short analysis, which guaranties to filter out interfering aftershocks and other nuisances, is performed on the smoothed envelope data (2 s Bartlett window). If the final coda window is shorter than 8 s, e.g. because the signal-to-noise ratio is quickly reached, data for this station is removed from the inversion. If data of less than 3 stations is remaining, the corresponding frequency band is completely removed from the analysis for this event. Data in the direct wave window is av-

eraged. Furthermore, observed and modeled envelopes are smoothed with a 2 s wide Bartlett window. Finally, the inversion for intrinsic and scattering attenuation as well as site effects and spectral source energy is performed by solving the least-squares linear equation system $E_{obs} = E_{mod}$ for given g^* and simultaneous optimization of g^* as described in *Eulenfeld and Wegler* [2016]. The weight of the S-wave window in the inversion corresponds to its width.

Envelope fits for two representative earthquakes are displayed in Figure 2. The epicenters of the two earthquakes are marked with white crosses in figure 1. The western event is located in a low scattering environment and the eastern event in a high scattering environment. The fits exemplify that stronger scattering mainly manifests in a lower ratio between energy density levels of direct S-wave and coda, while intrinsic attenuation accounts for a linear decrease of the logarithm of energy density with time.

2.2 Accumulation of observations and correction of site responses

The analysis of the previous section is repeated for each of the around 45 000 events. Around 21 000 events are discarded, because not enough stations are deployed in less than 110 km distance at the time of event occurrence or because other of the above defined criteria are not met. The values of Q_i^{-1}, Q_{sc}^{-1} and R for each event are associated with the corresponding stations. For easier analysis observables are log scaled with base 10 in the following. The robust mean [*Eulenfeld and Wegler*, 2016; *Huber*, 2014] and the median absolute deviation (MAD) of the observables are calculated for each station. The MAD is utilized as error of the corresponding observables. As an example, results for scattering attenuation at a central frequency of 6 Hz are displayed in the left panel of Figure 3. Slopes are calculated for the attenuation observables by fitting a line to the averaged log-log scaled measurements.

To resolve any ambiguity in the solution of the equation system because of the collinearity of W and R_i in equation 2, the geometric mean of site responses at used stations is set to 1. As a result, site responses obtained from different events may not be compared. The discrepancy is resolved by a second inversion for site responses and spectral source energies leaving attenuation parameters Q_i^{-1} and Q_{sc}^{-1} untouched. Therefor, a linear equation system is constructed by assuming that site amplification factors for one station and frequency are the same for different events [eq. 10 in *Eulenfeld and Wegler*, 2016]. The equation system is split into independent sub-systems each corresponding to an area of stations connected by measurements of different events. Only the sub-system of the largest contiguous area is solved with the method of least squares. Site amplification measurements for the smaller areas are discarded as it is difficult to determine how the values between different contiguous areas are aligned to each other. The geometric mean of site responses is again fixed to 1 to resolve ambiguity, but this time all measurements of the largest contiguous area are involved. The number of unknowns equals the number of overall used events. The number of equations equals approximately the sum of the number of observations over all stations in the largest contiguous area. In our case, the coefficient matrix has around 25 000 columns (unknowns) and 75 000 to 110 000 rows (equations) depending on frequency. Luckily, the coefficient matrix is sparse with a density around 0.01% which allows to solve the equation system with specially designed efficient algorithms. We use the Qopen implementation to correct site responses. Qopen employs the LSMR algorithm [*Fong and Saunders*, 2011] by means of the SciPy [*Jones et al.*, 2011-] submodule `scipy.sparse`. Exemplary, results of this procedure are displayed in Figure 4 showing energy site amplification factors before and after the correction.

2.3 Performing the interpolation

Before the interpolation, results are discarded for a specific station and frequency band if less than 4 observations are available. In the left plot of figure 3 discarded stations are encircled red. The slope of an attenuation observable at a station is only used if the corresponding attenuation observable is available at more than 3 frequencies.
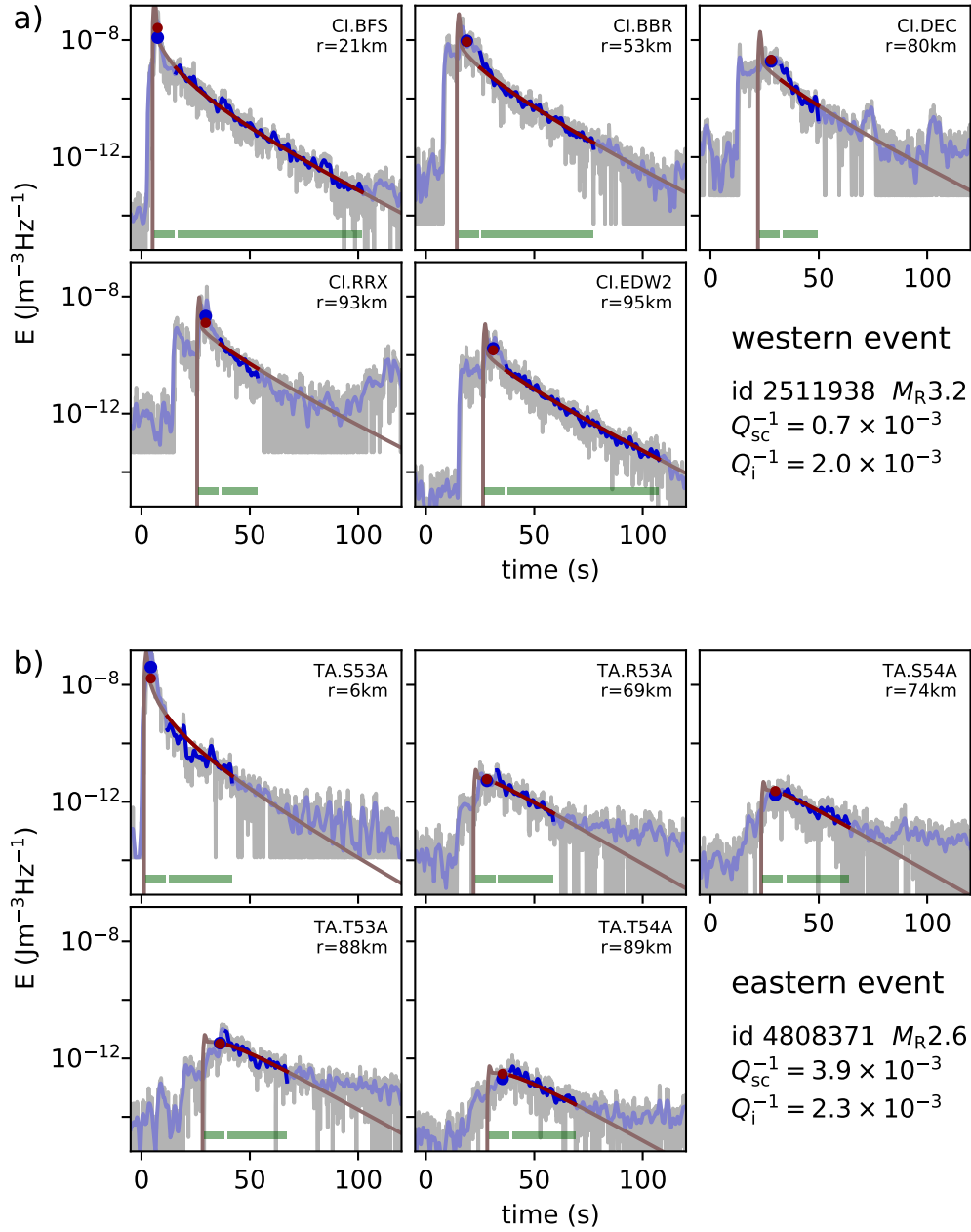
Figure 2. Envelope fits between observed and modeled energy densities for the inversion of two different earthquakes (event ids indicated) in the frequency band from 4 Hz to 8 Hz. Displayed in each panel are the observed envelope (gray), the smoothed observed envelope (blue) and the smoothed modeled envelope (red). S-wave and coda window are indicated with green bars. The mean of the observed and modeled envelope in the S-wave window is indicated with a blue and red dot, respectively. Station name and distance to hypocenter is indicated in each panel. The epicenter locations for the western (panel a) and eastern event (panel b) are indicated in figure 1. Intrinsic attenuation is similar for both events, but scattering is stronger for the eastern event manifesting in a lower ratio between energy density levels of direct S-wave and coda.
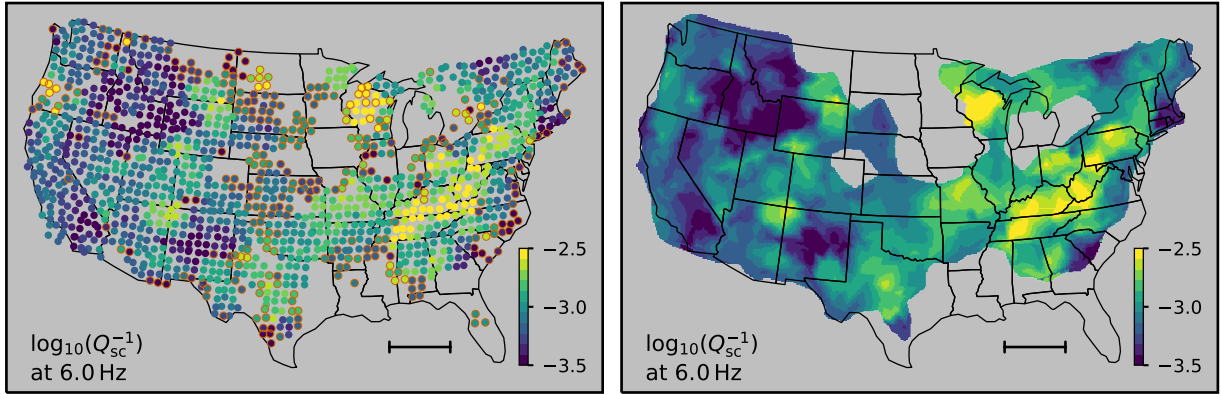
Figure 3. Map of shear wave scattering attenuation at 6 Hz measured at the USArray stations (left) and interpolated (right). Measurements encircled red in the left plot are discarded because of the low number of observations.
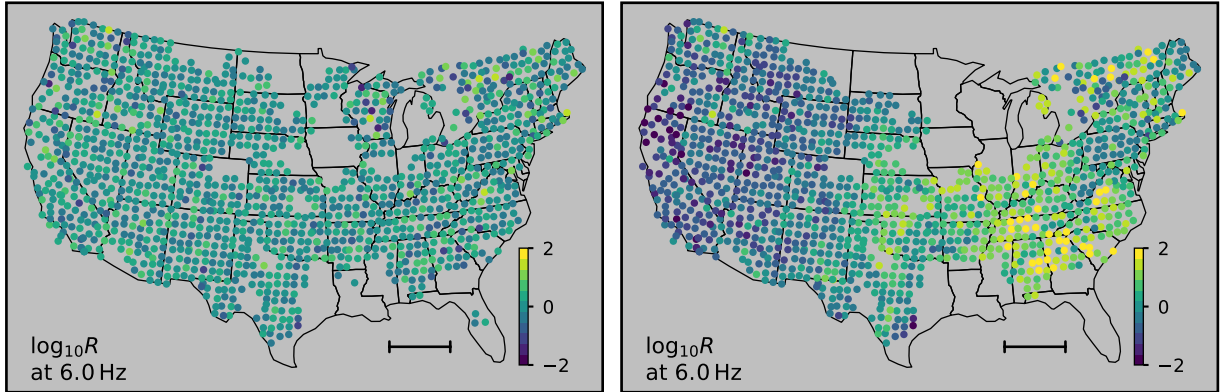
Figure 4. Map of energy site amplification factors at 6 Hz before (left) and after (right) correction of the values. In the left plot the geometric mean of energy site amplifications is fixed for each inversion of an earthquake. Different measurements of the site amplification are therefore not comparable. Contrary, in the right plot the geometric mean of all energy site amplification measurements is fixed allowing to compare site amplification factors at different locations. Note, that the right plot only displays observations at stations inside the largest contiguous area (see main text).

The interpolation of observables between station locations works as follows: Firstly, the interpolation area has to be defined with care because of the large holes without earthquake activity. We calculate concave hulls by performing a Delaunay triangulation between station locations and subsequently removing all triangles with a circumradius larger than 150 km (alpha value of alpha shape). The concave hulls formed by the remaining triangles are enlarged by 50 km in all possible directions to define the interpolation area. For the interpolation inside the convex hull of the station locations, again the Delaunay triangulation is applied. Following, linear barycentric interpolation is performed in each triangle. Outside the convex hull the interpolation area is filled with the value of the respective nearest station. For this purpose, the SciPy function `scipy.interpolate.griddata` with `method='linear'` and `method='nearest'` is used. Exemplary, figure 3 shows scattering attenuation at a central frequency of 6 Hz before and after interpolation. The interpolated number of observations at 6 Hz is displayed in figure 1.

3 Results

We obtained measurements at around 1400 of the 1844 used stations. Results for interpolated log-scaled intrinsic and scattering attenuation $\log_{10} Q^{-1}$ are displayed in Figure 5 at the central frequencies 1.5 Hz, 3 Hz, 6 Hz, and 12 Hz. The slopes of frequency-dependent intrinsic and scattering attenuation are displayed in Figure 6. Log-scaled energy site amplification factors $\log_{10} R$ are displayed in Figure 7 at the above mentioned frequencies. Note, that site amplification values of one frequency can be compared with each other, but a statement about the absolute value is not possible.

Furthermore, we provide an extensive electronic supplement containing all results in re-usable and demonstrative format:

1. PDF figures of total, intrinsic and scattering attenuation, seismic albedo, energy site amplification and number of observations as well as corresponding errors if applicable. Each figure consists of plots of results per station and plots of interpolated results for the central frequencies 1.5 Hz, 3 Hz, 6 Hz, 12 Hz. Plots of the slope are displayed if applicable.
2. Results per station for all analyzed frequencies in JSON format. The configuration file for the Qopen package is provided, too.
3. Interpolated observables for all analyzed frequencies in georeferenced TIF format.
4. The JavaScript application *Qviewer* to explore all results interactively. It allows to display observables as a function of frequency at a single station.

The resolution of our observations is governed by the inter-station spacing of around 70 km and the restriction of the event-station distance to a maximum of 110 km. We expect therefore a resolution around 100 km. For comparison, the length of the scale bar in the displayed maps is 500 km. Two indicators for the accuracy of our results are available. Firstly, the number of observations correlating with the areal event density and secondly the median absolute deviation (MAD) as a measure for the spread of the distribution of observations. Active regions as large parts of the western United States, Appalachian and Interior Highlands show a high number of observations (figure 1). Other regions have a low number of observations, e.g. the Central Lowland, Coastal Plain, and New England, results from these regions should be regarded with caution. Errors (MAD) are provided in the electronic supplement. It has to be noted that results might be slightly obscured by the different depths of used earthquake origins.

Figure 5 reveals a distinct west-east decline for intrinsic attenuation at all frequencies above 1.5 Hz. Regions with low intrinsic attenuation for most frequencies are the High Plains (especially the Llano Estacado), the imaged part of the Coastal Plain, and Sierra Nevada. Regions with high intrinsic attenuation are the Pacific Border province, Boston Mountains (part of the Interior Highlands), Southern Rocky Mountains, and the area around the Great Salt

Lake. Scattering depicts a raising west-east trend for frequencies higher than 3 Hz, but generally has a higher spatial variation than intrinsic attenuation. High scattering is observed in the Early Tertiary part of the Missouri Plateau, Navajo Section of Colorado Plateaus, Superior Uplands (high frequencies) and large parts of the Interior Plains and Appalachian Highlands. Low scattering is observed at Columbia Plateau and Northern Rocky Mountains, Sierra Nevada and Southern California, Pecos Valley (Great Plains) and Mexican Highland (Basin and Range province), and mapped parts of the Coastal Plain including the Lower Mississippi Region. The slope of the frequency dependence of attenuation shows a raising west-east trend for intrinsic attenuation and a decreasing west-east trend for scattering attenuation (figure 6). A correlation is observed between the slopes and attenuation values at 1.5 Hz for intrinsic and scattering attenuation. At 1.5 Hz scattering attenuation and intrinsic attenuation dominate variantly in the United States. Interestingly at higher frequencies a pattern can be observed: In the western part intrinsic attenuation is dominant except for Missouri Plateau and Navajo section of Colorado Plateaus. In the Eastern part scattering attenuation is dominant except for the eastern rim of the imaged area. The border between the domination of intrinsic and scattering attenuation is at a longitude of around 103°W which is near the boundary of Interior plains and Rocky Mountains. Geometric averages of intrinsic, scattering and total attenuation over the whole study area as a function of frequency are displayed in Figure 8. The total Q value can be approximated by $Q_{tot} = 59 \times f^{1.0}$. Additionally, the geometric mean of total, intrinsic and scattering attenuation is displayed for the western and eastern part of US (border at 103°W) to illustrate further the above mentioned west-east trends.

For energy site amplification factors, it has to be noted, that site amplification is highly influenced by the material near the surface and depends strongly on the exact location of the seismometer as site amplification can vary over short distances. Therefore, we report only large-scale variations in site amplification factors (figure 7). At low frequencies the site amplification is relatively uniform with some distinct areas (e.g. High Plains). For higher frequencies, a west-east trend of rising site amplification values is visible. Energy site amplifications reach levels up to 100 corresponding to an amplitude site amplification of 10. Southern parts of the Appalachian Highlands show a higher site amplification than the northern parts.

Source displacement spectra of the earthquakes are calculated from the spectral source energies W as a function of frequency [*Eulenfeld and Wegler*, 2016, eq. 11]. Moment magnitudes M_w are estimated with the geometric mean of the source displacement spectrum at frequencies smaller than 6 Hz. Source displacement spectra, seismic moments and moment magnitudes for all analyzed events are provided in the electronic supplement. We compare estimated moment magnitudes with moment magnitudes obtained by moment tensor inversions of different institutions in Table 1. Due to the small overlap in the magnitude range, only 22 events were processed both by one of the institutions and ourselves. Before the correction of site responses, our moment magnitudes show an acceptable agreement with the reference magnitudes with a mean deviation of 0.16 and a slight positive systematic shift (mean signed deviation). After the correction for site responses, moment magnitudes are systematically over-estimated. This is because the mean site amplification of 1 over the whole US was chosen arbitrary and most of the compared earthquakes ruptured in western US areas with low site amplification. A clear trade-off between spectral source energies and assumed averaged site amplification exists. For example, if we assumed a mean energy site amplification of 8 (amplitude factor 2.8) all estimated moment magnitudes would be reduced by 0.28. This completely eliminates the systematic deviation and results in a mean deviation of 0.13.

A comparison of estimated moment magnitudes after site correction and local Richter magnitudes M_R reported by the Array Network Facility (ANF) is displayed in Figure 9 in two panels for western and eastern US. The relationship between determined moment magnitudes and Richter magnitudes is different for western and eastern US. We checked that this is not solely a side effect of the correction of site amplification. We compare our results to linear
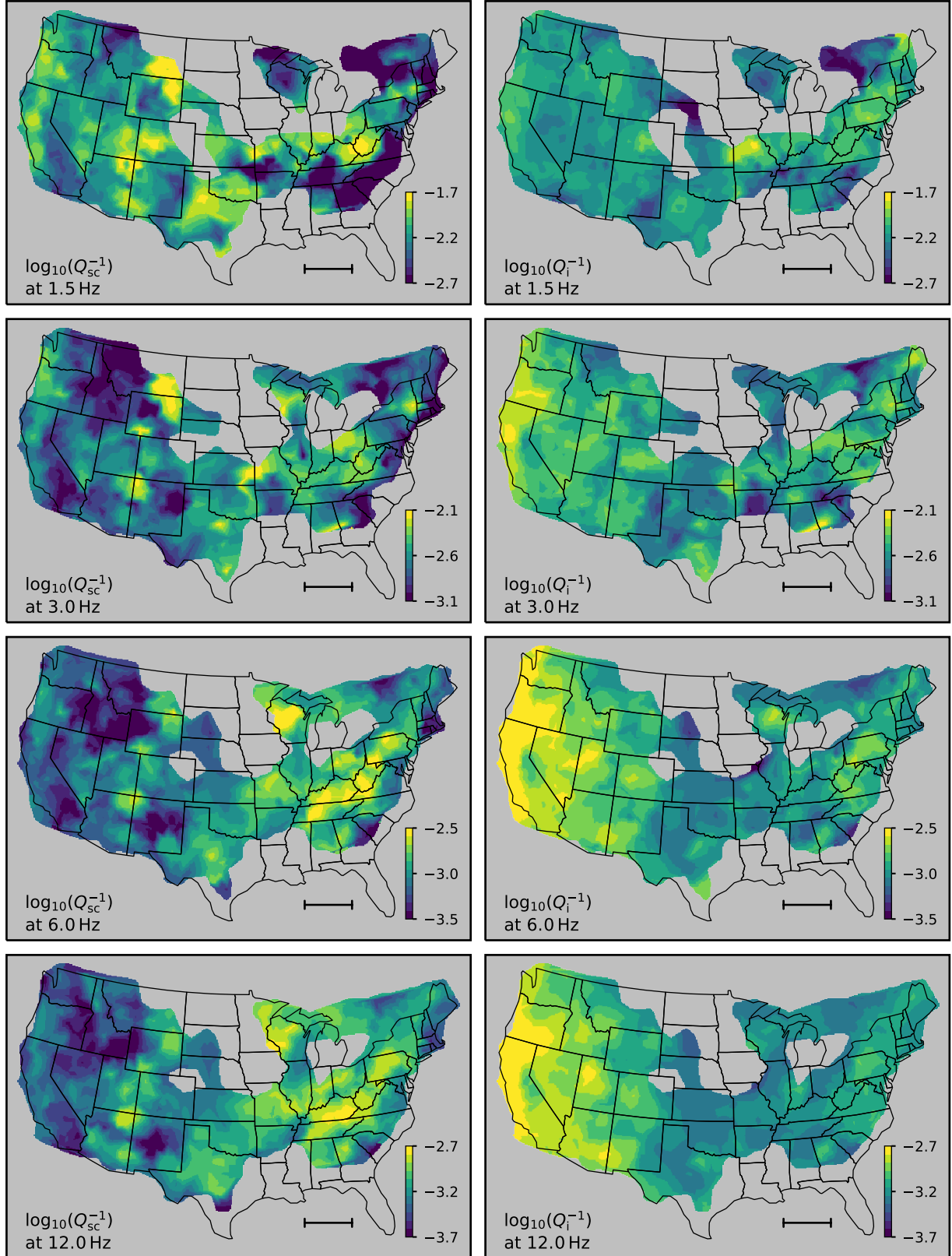
Figure 5. Comparison of crustal shear wave scattering attenuation (left) and intrinsic attenuation (right) at the central frequencies 1.5 Hz, 3 Hz, 6 Hz, and 12 Hz. Blue depicts low attenuation, yellow depicts high attenuation.
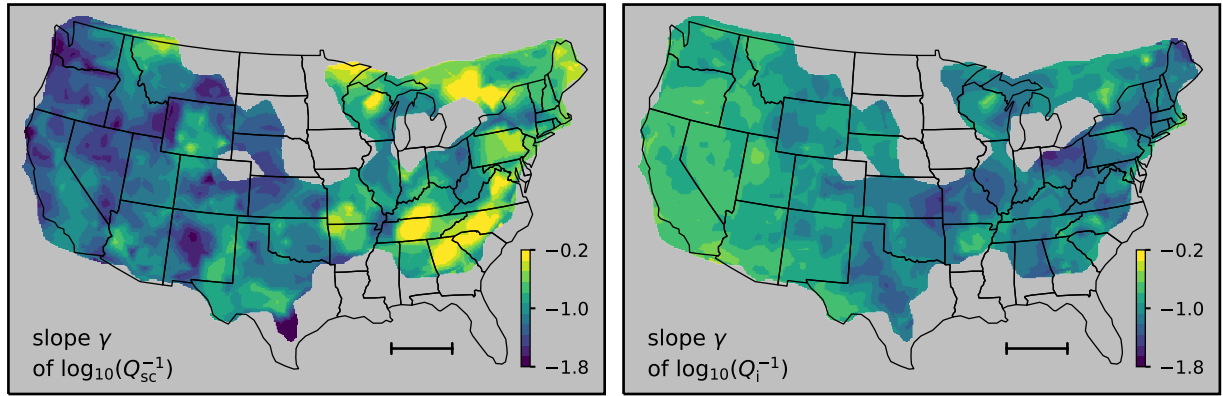
Figure 6. Slope of frequency dependence of shear wave scattering attenuation (left) and intrinsic attenuation (right).
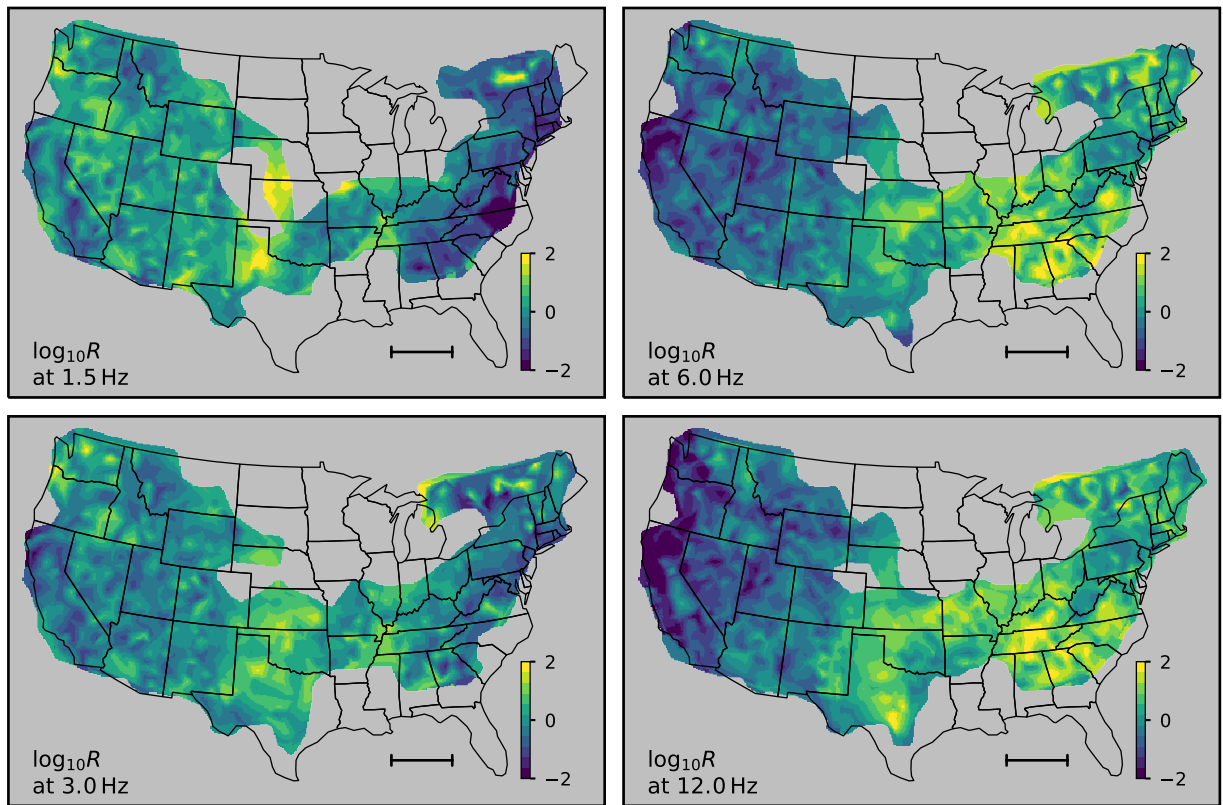
Figure 7. Energy site amplification at the central frequencies 1.5 Hz, 3 Hz, 6 Hz, and 12 Hz.

$$Q_{tot} = 59 \times f^{1.0}$$
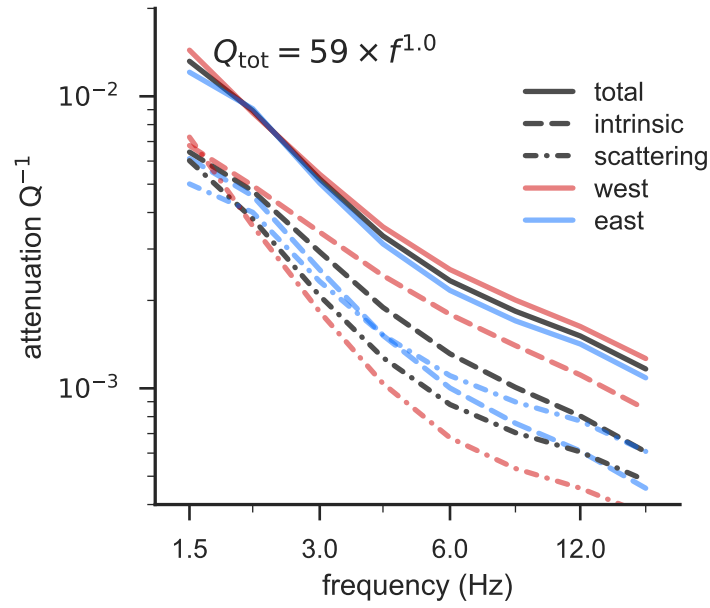
Figure 8. Mean of intrinsic, scattering and total attenuation for the whole study area and for the western and eastern part of the US as a function of frequency. Intrinsic attenuation dominates clearly in the West at all frequencies (except at 1.5 Hz) whereas in the eastern part this is only the case for low frequencies and scattering attenuation is more important at high frequencies.
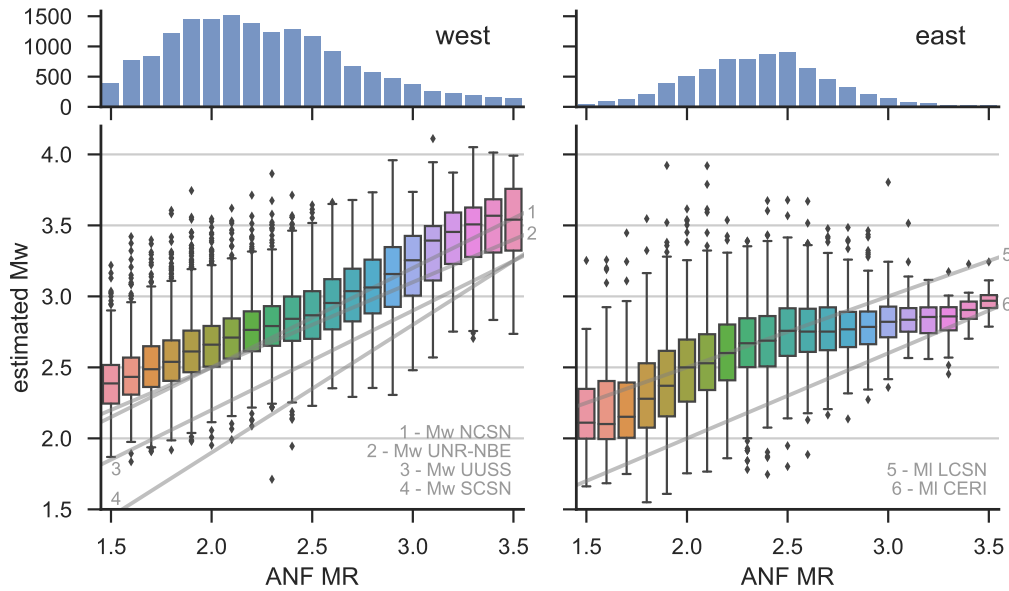
Figure 9. Box plots of the estimated moment magnitudes versus Richter local magnitudes reported by the Array Network Facility (ANF) for the western and eastern part of the US. The top panels show the number of events for each reported local magnitude. Opaque gray lines show linear fits between magnitudes from different agencies and Richter magnitudes [*Astiz et al.*, 2014].

–12–

Table 1. Comparison of estimated moment magnitudes with moment magnitudes derived by moment tensor inversion of different institutions. An acceptable mean deviation of 0.16 can be observed before the correction of site responses. In the main text we explain, why moment magnitudes are systematically higher after the correction.

ANF id	origin time	latitude (°)	longitude (°)	depth (km)	ref catalog	ref Mw	our Mw uncorrected	our Mw corrected
2013291	2005-04-16 10:13:15	35.891	-120.434	8.6	Berkeley[a]	3.45	3.76	3.83
1968787	2005-05-08 10:35:55	37.836	-122.226	5.0	Berkeley	3.29	3.41	3.67
2154477	2005-09-24 11:25:16	37.830	-122.221	5.4	ISC[b] BRK	3.2	3.33	3.57
2127896	2005-11-17 08:55:05	38.814	-122.783	2.4	Berkeley	3.88	3.67	3.99
2519807	2007-04-19 03:52:44	39.441	-123.106	4.8	Berkeley	3.5	3.42	3.94
2427335	2007-05-07 07:52:58	40.767	-121.562	8.7	ISC BRK	3.6	3.60	3.82
2482627	2007-05-20 23:10:19	37.364	-121.727	6.8	Berkeley	3.5	3.58	3.81
2525607	2007-05-26 08:04:12	37.419	-118.526	8.7	ISC BRK	3.3	3.39	3.54
2580402	2007-08-15 07:13:10	37.803	-122.193	5.7	Berkeley	3.2	3.32	3.62
2854061	2008-08-30 22:06:15	41.674	-111.145	2.8	SLU[c]	3.4	3.46	3.49
2867342	2009-03-21 08:47:50	43.322	-110.718	5.0	SLU	3.1	3.52	3.63
2867504	2009-03-25 07:51:23	33.290	-115.721	4.4	ISC PAS	3.6	3.39	3.73
2868918	2009-05-01 01:34:02	36.865	-104.864	6.6	SLU	3.5	3.21	3.22
2871933	2009-07-20 12:10:19	33.116	-116.207	14.5	ISC PAS	3.4	3.56	3.85
3343295	2012-05-18 16:51:17	37.203	-118.113	6.5	ISC NCEDC	3.2	3.35	3.34
3379316	2012-08-29 13:01:50	36.012	-118.403	4.8	Berkeley	3.38	3.49	3.77
4488469	2013-10-10 01:34:23	35.659	-118.472	10.6	Berkeley	3.34	3.50	3.72
4723074	2014-06-25 22:01:36	35.816	-119.880	9.3	Berkeley	3.37	3.68	3.69
					mean signed deviation		0.08	0.28
					mean absolute deviation		0.16	0.31

[a] UC Berkeley Seismological Laboratory [*NCEDC*, 2014]

[b] *International Seismological Centre* [2014]

[c] Saint Louis University Earthquake Center [*Herrmann*, 2013]
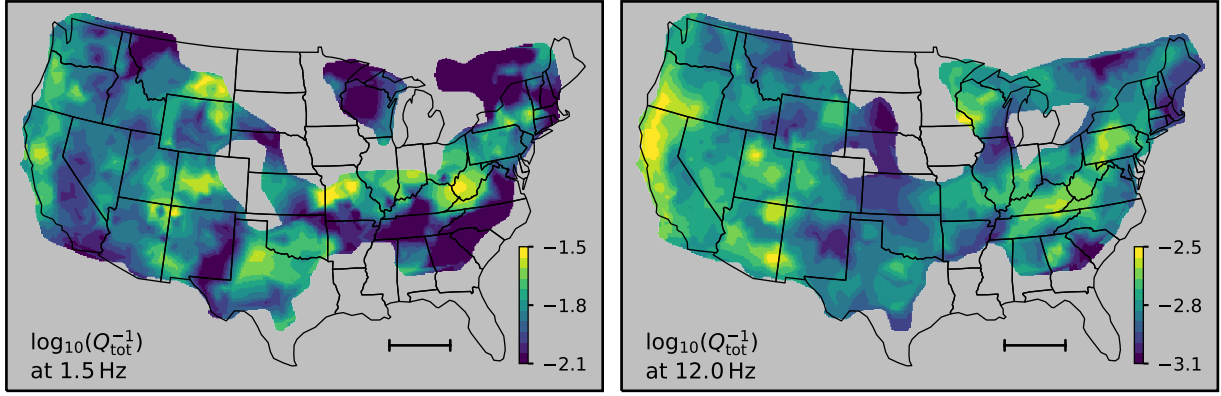
Figure 10. Total attenuation at 1.5 Hz and 12 Hz for the study area.

fits between moment magnitudes (west) respective local magnitudes (east) and Richter magnitudes. These fits are reported in figures S07 and S06b in the electronic supplement of *Astiz et al.* [2014]. Our relationship between moment magnitude and Richter magnitude in the west agrees well with the fit to moment magnitudes determined by the Northern California Seismic Network (NCSN). In the east the best agreement is with the fit to local magnitudes determined by Lamont-Doherty Cooperative Seismographic Network (LCSN). Fits to magnitudes reported by other agencies are systematically on a lower level. Please note that assuming a mean site amplification larger than 1 over the whole US (e.g. 8 as above) reduces our estimates by a constant factor, effectively creating a larger agreement between our M_w–M_R relationship and those of other institutions.

## 4 Comparison with other works and discussion

The west-east decline of intrinsic attenuation at all frequencies above 1.5 Hz is consistent with previous studies [e.g. *Mitchell*, 1995]. Its origin can be explained by a comparison to the heat flow map compiled by *Blackwell et al.* [2011] which shows a positive correlation to intrinsic attenuation. The values with the largest heat flow in the Western US (Yellowstone and Snake River plain, the area around Great Salk Lake, Southern Rocky Mountains) also show a relatively high intrinsic attenuation. An exception to this observation is the Great valley which has a low heat flow but no lower intrinsic attenuation than the surrounding. The west-east trend of intrinsic attenuation and heat flow reflects the transition from young, hot rock to old and cold rock. The heat anomaly in South Dakota is not reflected by intrinsic attenuation, because it is caused by large-scale ground-water flow from west to east [*Blackwell et al.*, 1991].

The scattering strength allows to conclude on the extent of crustal heterogeneity of S-wave velocities. Interesting insights might be obtained for the different geologic formations: For example, the young Quaternary and Tertiary sedimentary rocks of the Coastal Plain are more homogeneous on length scales down to 200 m (f=15 Hz at v_S=3.3 km/s) than the older Paleozoic sedimentary rocks of the Central Plains. Also, the crust in the western part of the United States appears to be more homogeneous on the relevant length scales than the crust in the eastern part. A reason might be, that heterogeneities in the hot and viscous (high Q_i^{-1}) rocks in the west are healing and mixing easier than in the cold and stiff rocks in the east. These healing and mixing processes seem to be more important than the creation of new cracks by active tectonics in the west.

This is the first time, intrinsic and scattering attenuation are reported separately for large regions of the US. To compare our results with previous attenuation measurements in the US area, maps of total attenuation at a central frequency of 1.5 Hz and 12 Hz are displayed in Figure 10. *Phillips and Stead* [2008] conducted a Lg attenuation tomography for Western US and report Q_{tot}. They windowed the Lg phase with group velocities of 3.6 km/s to 3.0 km/s. Results in the 0.75 Hz to 1.5 Hz frequency band are consistent in some regions and disagree in other regions to our results at a central frequency of 1.5 Hz. Several features match, e.g. high attenuation in the Pacific border region and near Yellowstone, low attenuation at the Columbia plateau and Northern Rocky Mountains. Other features do not match, most prominently the part of the Colorado plateaus showing a low attenuation in the study of *Phillips and Stead* [2008] but a high attenuation due to scattering in our study. *Phillips et al.* [2013] extend the study region of *Phillips and Stead* [2008] eastwards and report low attenuation in the Great plains province. This can be partly confirmed by our study. Controversially, our study shows higher attenuation in the parts of the Great Plains where scattering contributes significantly to the attenuation. It can be speculated that the mentioned Q attenuation studies of the Lg wave are mainly sensitive to intrinsic attenuation due to the guided nature of the Lg phase. Also, Lg wave attenuation is affected by topographic changes of the free surface and subsurface interfaces. *Gallegos et al.* [2014] performed the Lg attenuation tomography for the Central and Eastern US. They chose a 0.6 km/s wide, visually picked lapse time window. The correlation to our findings is not clear. A possible reason could be the existence of Paleozoic sedimentary basins which might substantially influence Lg attenuation.

Adams and Abercrombie [1998] estimated intrinsic and scattering attenuation around Cajon Pass, southern California, with multiple lapse time window analysis (MLTWA). In Figure 11a we compare their results for station CSP and borehole station CJP with our observations at near-by station CI.BFS and with results at station CJP from *Leary and Abercrombie* [1994]. There is a very good agreement of observed intrinsic attenuation in all studies with small deviations at low frequencies. The scattering estimates of *Leary and Abercrombie* [1994] show a clear offset from the other measurements. This can be explained due to the single scattering assumption they used. Multiple scattering models employed in *Adams and Abercrombie* [1998] and our study add additional energy to the coda from multiple scattered waves [*Gao et al.*, 1983]. The same coda envelope therefore has to be explained with stronger scattering in a multiple scattering description. Estimates of scattering in *Adams and Abercrombie* [1998] fit well to our observations for the CJP stations and estimates are a bit higher but follow the same frequency dependence for the CSP station. The slight discrepancy might be observed simply due to the different stations used. Intrinsic and scattering attenuation were also estimated by *Mayeda et al.* [1992] for the Long Valley and a part of Central California and by *Jin et al.* [1994] for Southern California. We compare these studies to the 0, 25, 50, 75 and 100 percentiles at 83 stations in Southern and Central California in Figure 11b. Our results show a good agreement with the study of *Jin et al.* [1994] for Southern California. On the other hand, a slight discrepancy between our results and the estimates of *Mayeda et al.* [1992] is visible, especially for the Long Valley. The USArray station CI.MLAC is located inside the Long Valley Caldera, but the resolution of our results ($\approx$ 100 km) is larger than the extent of the presumably high scattering caldera ($\approx$ 30 km) which can explain the differences in the two measurements. The higher scattering strength for Central California compared to Southern California can be verified by our study (compare figure 5). These comparisons with MLTWA studies confirm that we can be confident in our attenuation results especially for regions with a large number of observation.

The procedure we used to correct for site responses uses the strong assumption of isotropic source radiation patterns of individual earthquakes which is of course not fullfilled. We expect that this assumption does not affect results for regions with a lot of earthquakes with different radiation patterns. Serious errors may be introduced in regions with a low number of earthquakes or in regions with a dominating moment tensor. These errors can propagate to neighboring regions due to the correction algorithm. This effect plays a larger
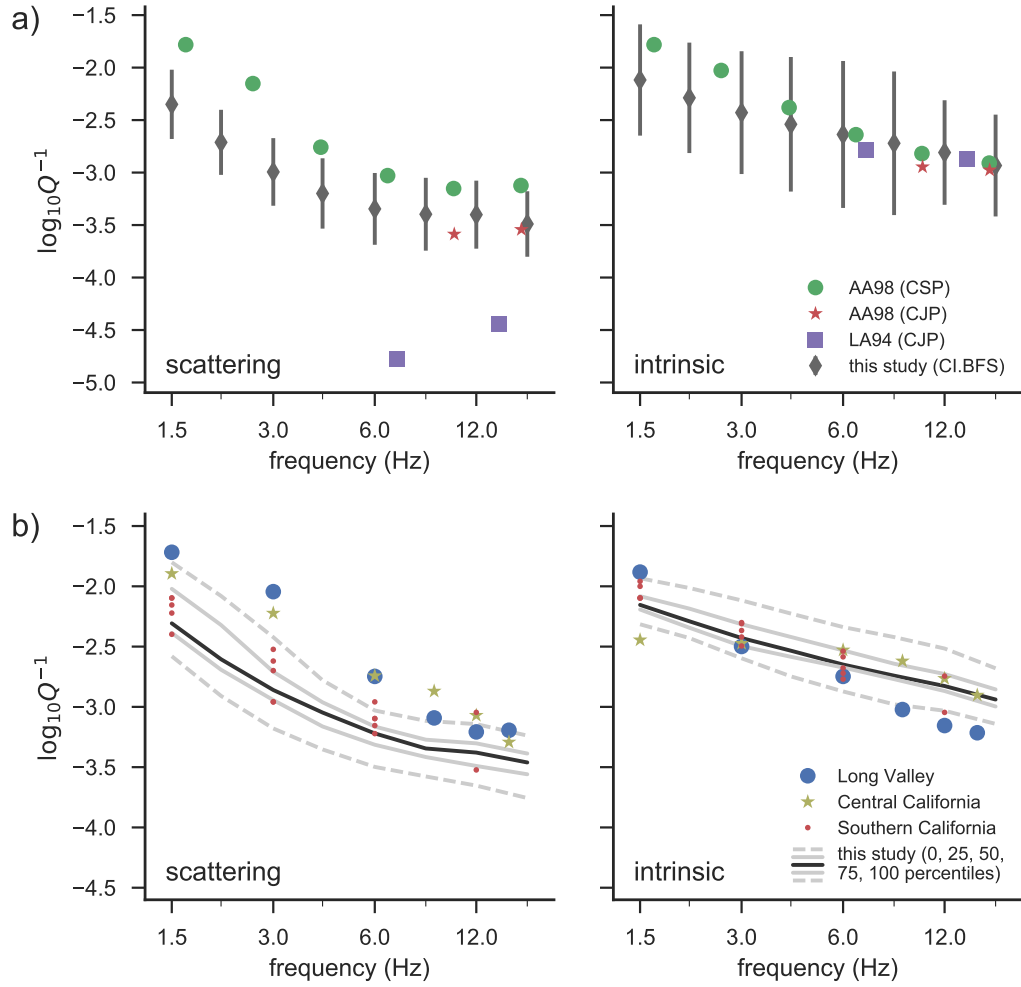
Figure 11. a) Comparison of estimates of scattering (left) and intrinsic attenuation (right) from station CI.BFS of our study and studies of nearby stations by *Adams and Abercrombie* [1998] and *Leary and Abercrombie* [1994]. b) Comparison of estimates of scattering (left) and intrinsic attenuation (right) for Central and Southern California. Displayed are the median (black line), 25 and 75 percentiles (gray lines), and minimum and maximum (gray dashed lines) of all stations in Central and Southern California for each frequency. We compare our results to estimates at Long Valley, Central California [*Mayeda et al.*, 1992] and Southern California [*Jin et al.*, 1994].

role for low frequencies and might render site amplification plots useless for low frequencies. Contrary, *Takemura et al.* [2009] show that at higher frequencies (>5 Hz) higher scattering counterbalances the anisotropic radiation pattern. This argument is supported by our observation that the alignment was more successful for higher frequencies than for lower frequencies: The reduction of the mean of the standard deviations of site amplification observations at individual stations due to the alignment is around 3% to 4% for frequencies smaller than 5 Hz and around 8% to 10% for frequencies higher than 5 Hz. The absolute value of the mean standard deviation is also higher at low frequencies (0.5-0.6 compared to 0.45 at higher frequencies). We are therefore confident, that the west-east increase of high frequency energy site amplification and the extraordinary high value at the Interior Low Plateaus and the southern part of the Appalachian Highlands are reliable results. The high site amplification might be connected to the high scattering strength in the same region. v_{S30} maps (mean S-wave velocity over top 30 m) derived from topographic slopes [*Wald and Allen*, 2007] show a similar trend as our site amplification maps (higher v_{S30} values in large parts of eastern US). In detail, deviations are observed. The resolution of our maps is limited by the average distance between US array stations (70km). On the other hand, topographic slope is only a proxy for v_{S30} which itself is a weak proxy for site amplification [*Castellaro et al.*, 2008], whereas we directly measure frequency dependent site amplification.

For estimating the seismic moment our method [based upon *Sens-Schönfelder and Wegler*, 2006] only needs data of the earthquake itself. This can be an advantage to the previous coda method of *Mayeda and Walter* [1996] using Empirical Green's function corrections. The good agreement between our estimates and independently derived moment magnitudes in table 1 therefore is promising. Estimates of moment magnitude for different events with the same Richter magnitude scatter a lot in figure 9 because Richter magnitudes for different regions inherently correspond to different moment magnitudes, e.g. due to different attenuation or varying stress drops of the earthquakes. Additionally, if g^* or b are determined erroneously for a single event, W and the reported moment magnitude are affected. One reason for the observed difference in magnitude scaling in west and east is the higher intrinsic attenuation in the west. The same ground motions (proportional to Richter magnitude) then originate from more powerful sources (proportional to moment magnitude). Estimated moment magnitudes in the west are therefore larger for similar Richter magnitudes. This effect is even larger for stronger earthquakes, because more stations which are further away contribute to the M_R calculation and waves are damped proportional to Q^{-1} and travel time. One might argue that the difference should be manifested by total attenuation, but this can only be true when the direct wave which attenuates with Q_{tot}^{-1} dominates the calculation of the Richter magnitude. For higher scattering media as in the Southern Appalachian Highlands the coda dominates the recordings and the influence of intrinsic attenuation on Richter magnitude calculation surpasses the influence of scattering attenuation. Another reason for the different magnitude scaling in west and east are potentially higher stress drops for eastern earthquakes [e.g. Mw 5.7 Virginia earthquake, *Ellsworth et al.*, 2011] than for western earthquakes [e.g. *Allmann and Shearer*, 2007]. A higher stress drop for an earthquake with the same seismic moment M_0 implies a smaller fault area and a shorter time function resulting in higher corner frequency and larger shaking and thus larger M_R. Furthermore, the higher site amplification for high frequencies in the east might be of importance, especially for earthquakes of high stress drops and high corner frequency.

Differences between the magnitude relationship presented in figure 9 and the fits from *Astiz et al.* [2014] might be due to the fact, that most of the latter are only calculated for larger events depending on the completeness of the reference catalog. Furthermore, the mean energy site amplification does not equal the assumed value of 1 and it might be different for different frequencies. For example, a mean energy site amplification factor of 10 (amplitude factor 3.1) would result in a moment magnitude reduction of 0.3 in our results. The flattening of the moment magnitude-Richter magnitude relationship in the East for $M_R > 2.5$ might be another indication of varying stress drops of different earthquakes in eastern US areas.

5 Conclusions

We presented the areal distribution of crustal S-wave intrinsic and scattering attenuation for the contiguous United States as a function of frequency between 1 Hz and 20 Hz. This is the first time, intrinsic attenuation and scattering attenuation were separated and mapped for a large part of the United States. Because we used a simple homogeneous model, reported Q values should be interpreted as an crustal average between used earthquakes and stations. The most prominent feature we identified is the declining west-east trend of intrinsic attenuation and the raising west-east trend of scattering strength. Furthermore, energy site amplification factors were reported. Our findings of a high site amplification at some regions in the east at frequencies above 5 Hz should be further hardened or rebutted by independent investigations. The good agreement between estimated moment magnitudes and independently derived moment tensors confirm the robustness of the Qopen inversion algorithm. Differences between moment magnitudes and ANF reported Richter magnitudes can be explained reasonably well. We provide an extensive electronic supplement which allows an easy comparison of future studies with our findings.

References

Adams, D. A., and R. E. Abercrombie (1998), Seismic attenuation above 10 Hz in southern California from coda waves recorded in the Cajon Pass borehole, *Journal of Geophysical Research: Solid Earth*, *103*(98), 24,257–24,270.

Allmann, B. P., and P. M. Shearer (2007), Spatial and temporal stress drop variations in small earthquakes near Parkfield, California, *Journal of Geophysical Research: Solid Earth*, *112*(4), 1–17, doi:10.1029/2006JB004395.

Astiz, L., J. A. Eakins, V. G. Martynov, T. A. Cox, J. Tytell, J. C. Reyes, R. L. Newman, G. H. Karasu, T. Mulder, M. White, G. A. Davis, R. W. Busby, K. Hafner, J. C. Meyer, and F. L. Vernon (2014), The Array Network Facility Seismic Bulletin: Products and an Unbiased View of United States Seismicity, *Seismological Research Letters*, *85*(3), 576–593, doi:10.1785/0220130141.

Blackwell, D., J. Steele, and L. Carter (1991), Heat-flow patterns of the North American continent; A discussion of the Geothermal Map of North America, in *Neotectonics of North America*, edited by D. Slemmons, E. Engdahl, M. Zoback, and D. Blackwell, chap. 23, pp. 423–436, Geological Society of America, Boulder, Colorado.

Blackwell, D. D., M. C. Richards, Z. S. Frone, J. F. Batir, M. A. Williams, A. A. Ruzo, and R. K. Dingwall (2011), SMU Geothermal Laboratory Heat Flow Map of the Conterminous United States, Supported by Google.org, Available at http://www.smu.edu/geothermal.

Burdick, S., C. Li, V. Martynov, T. Cox, J. Eakins, T. Mulder, L. Astiz, F. L. Vernon, G. L. Pavlis, and R. D. van der Hilst (2008), Upper Mantle Heterogeneity beneath North America from Traveltime Tomography with Global and USArray Transportable Array Data, *Seismological Research Letters*, *79*(3), 384–392, doi:10.1785/gssrl.79.3.384.

Carcolé, E., and H. Sato (2010), Spatial distribution of scattering loss and intrinsic absorption of short-period S waves in the lithosphere of Japan on the basis of the Multiple Lapse Time Window Analysis of Hi-net data, *Geophysical Journal International*, *180*(1), 268–

290, doi:10.1111/j.1365-246X.2009.04394.x.

Castellaro, S., F. Mulargia, and P. L. Rossi (2008), Vs30: Proxy for Seismic Amplification?, *Seismological Research Letters*, *79*(4), 540–543, doi:10.1785/gssrl.79.4.540.

Ellsworth, W. L., K. Imanishi, J. Luetgert, J. Kruger, and J. Hamilton (2011), The Mw 5.8 Virginia Earthquake of August 23, 2011 and its Aftershocks: A Shallow High Stress Drop Event, *AGU Fall Meeting Abstracts*.

Eulenfeld, T., and U. Wegler (2016), Measurement of intrinsic and scattering attenuation of shear waves in two sedimentary basins and comparison to crystalline sites in Germany, *Geophysical Journal International*, *205*(2), 744–757, doi:10.1093/gji/ggw035.

Fehler, M., M. Hoshiba, H. Sato, and K. Obara (1992), Separation of scattering and intrinsic attenuation for the Kanto-Tokai region, Japan, using measurements of S -wave energy versus hypocentral distance, *Geophysical Journal International*, *108*(3), 787–800, doi:10.1111/j.1365-246X.1992.tb03470.x.

Fong, D. C.-L., and M. Saunders (2011), LSMR: An Iterative Algorithm for Sparse Least-Squares Problems, *SIAM Journal on Scientific Computing*, *33*(5), 2950–2971, doi:10.1137/10079687X.

Gaebler, P. J., T. Eulenfeld, and U. Wegler (2015), Seismic scattering and absorption parameters in the W-Bohemia/Vogtland region from elastic and acoustic radiative transfer theory, *Geophysical Journal International*, *203*(3), 1471–1481, doi:10.1093/gji/ggv393.

Gallegos, A., N. Ranasinghe, J. Ni, and E. Sandvol (2014), Lg attenuation in the central and eastern United States as revealed by the EarthScope Transportable Array, *Earth and Planetary Science Letters*, *402*, 187–196, doi:10.1016/j.epsl.2014.01.049.

Gao, L. S., L. C. Lee, N. N. Biswas, and K. Aki (1983), Comparison of the effects between single and multiple scattering on coda waves for local earthquakes, *Bulletin of the Seismological Society of America*, *73*(2), 377–389.

Herrmann, R. B. (2013), Computer Programs in Seismology: An Evolving Tool for Instruction and Research, *Seismological Research Letters*, *84*(6), 1081–1088, doi:10.1785/0220110096.

Hoshiba, M., H. Sato, and M. Fehler (1991), Numerical basis of the separation of scattering and intrinsic absorption from full seismogram envelope. A Monte-Carlo simulation of multiple isotropic scattering., *Papers in Meteorology and Geophysics*, *42*(2), 65–91, doi:10.2467/mripapers.42.65.

Huber, P. J. (2014), Robust Statistics, in *International Encyclopedia of Statistical Science*, edited by M. Lovric, pp. 1248–1251, Springer Berlin Heidelberg, Berlin, Heidelberg, doi:10.1007/978-3-642-04898-2_594.

International Seismological Centre (2014), On-line Bulletin, http://www.isc.ac.uk, Internatl. Seismol. Cent., Thatcham, United Kingdom.

Jin, A., K. Mayeda, D. Adams, and K. Aki (1994), Separation of intrinsic and scattering attenuation in southern California using TERRAscope data, *Journal of Geophysical Research*, *99*(B9), 17,835–17,848, doi:10.1029/94JB01468.

Jones, E., T. Oliphant, P. Peterson, and Others (2011-), SciPy: Open Source Scientific Tools for Python, http://www.scipy.org/.

Krischer, L., T. Megies, R. Barsch, M. Beyreuther, T. Lecocq, C. Caudron, and J. Wassermann (2015), ObsPy: a bridge for seismology into the scientific Python ecosystem, *Computational Science & Discovery*, *8*(1), 014,003, doi:10.1088/1749-4699/8/1/014003.

Lacombe, C., M. Campillo, A. Paul, and L. Margerin (2003), Separation of intrinsic absorption and scattering attenuation from Lg coda decay in central France using acoustic radiative transfer theory, *Geophysical Journal International*, *154*(2), 417–425, doi:10.1046/j.1365-246X.2003.01976.x.

Leary, P., and R. Abercrombie (1994), Frequency dependent crustal scattering and absorption at 5-160 Hz from coda decay observed at 2.5 km depth, *Geophysical Research Letters*, *21*(11), 971–974, doi:10.1029/94GL00977.

Lin, F. C., B. Schmandt, and V. C. Tsai (2012), Joint inversion of Rayleigh wave phase velocity and ellipticity using USArray: Constraining velocity and density structure in the upper

crust, *Geophysical Research Letters*, *39*(12), 1–7, doi:10.1029/2012GL052196.

Mayeda, K., and W. R. Walter (1996), Moment, energy, stress drop, and source spectra of western United States earthquakes from regional coda envelopes, *Journal of Geophysical Research*, *101*(B5), 11,195–11,208, doi:10.1029/96JB00112.

Mayeda, K., S. Koyanagi, M. Hoshiba, K. Aki, and Y. Zeng (1992), A comparative study of scattering, intrinsic, and coda Q^{-1} for Hawaii, Long Valley, and central California between 1.5 and 15.0 Hz, *Journal of Geophysical Research*, *97*(B5), 6643–6659, doi: 10.1029/91JB03094.

Mitchell, B. J. (1995), Anelastic structure and evolution of the continental crust and upper mantle from seismic surface wave attenuation, *Reviews of Geophysics*, *33*, 441–462, doi: 10.1029/95RG02074.

NCEDC (2014), Northern California Earthquake Data Center, UC Berkeley Seismological Laboratory, Dataset, doi:10.7932/NCEDC.

Paasschens, J. (1997), Solution of the time-dependent Boltzmann equation, *Physical Review E*, *56*(1), 1135–1141, doi:10.1103/PhysRevE.56.1135.

Phillips, W. S., and R. J. Stead (2008), Attenuation of Lg in the western US using the USArray, *Geophysical Research Letters*, *35*(7), 1–5, doi:10.1029/2007GL032926.

Phillips, W. S., K. M. Mayeda, and L. Malagnini (2013), How to Invert Multi-Band, Regional Phase Amplitudes for 2-D Attenuation and Source Parameters: Tests Using the USArray, *Pure and Applied Geophysics*, *171*(3-5), 469–484, doi:10.1007/s00024-013-0646-1.

Sens-Schönfelder, C., and U. Wegler (2006), Radiative transfer theory for estimation of the seismic moment, *Geophysical Journal International*, *167*(3), 1363–1372, doi:10.1111/j.1365-246X.2006.03139.x.

Takemura, S., T. Furumura, and T. Saito (2009), Distortion of the apparent S-wave radiation pattern in the high-frequency wavefield: Tottori-Ken Seibu, Japan, earthquake of 2000, *Geophysical Journal International*, *178*(2), 950–961, doi:10.1111/j.1365-246X.2009.04210.x.

Wald, D. J., and T. I. Allen (2007), Topographic slope as a proxy for seismic site conditions and amplification, *Bulletin of the Seismological Society of America*, *97*(5), 1379–1395, doi:10.1785/0120060267.

Yang, Y., and M. H. Ritzwoller (2008), Characteristics of ambient seismic noise as a source for surface wave tomography, *Geochemistry, Geophysics, Geosystems*, *9*(2), doi:10.1029/2007GC001814.